Contact Area and Deformation of *Escherichia coli* Cells Adhered on a Cationic Surface

Zhou Xu,[1] Alexander Gamble,[2] Wuqi Amy Niu,[3] Morgan N. Smith,[3] M. Sloan Siegrist,[4,5] Mark Tuominen,[1] and Maria M. Santore[3,5]*

1. Department of Physics, University of Massachusetts, Amherst, MA 01003 USA
2. Department of Plant and Soil Science, University of Massachusetts, Amherst, MA 01003 USA
3. Department of Polymer Science and Engineering, University of Massachusetts Amherst, MA 01003 USA
4. Department of Microbiology, University of Massachusetts Amherst, MA 01003 USA
5. Molecular and Cellular Biology Graduate Program, University of Massachusetts, Amherst, MA 01003 USA

*corresponding author: Maria Santore
Department of Polymer Science and Engineering
University of Massachusetts
120 Governors Drive
Amherst, MA 01003 USA
413-577-1417
santore@mail.pse.umass.edu

Abstract

When bacteria adhere to surfaces, the chemical and mechanical character of the cell-substrate interface guides cell function and the development of microcolonies and biofilms. Alternately on bactericidal surfaces, intimate contact is critical to biofilm prevention. Direct study of the buried cell-substrate interfaces at the heart of these behaviors is hindered by the small bacterial cell size and inaccessibility of the contact region. Here we present a Total Internal Reflectance Fluorescence (TIRF) Depletion approach to measure the size of the cell-substrate contact region and quantify the gap separation and curvature near the contact zone, providing an assessment of the shapes of the near-surface undersides of adhered bacterial cells. Resolution of the gap height is about 10%, down to a few nanometers at contact. Using 1 and 2 μm silica spheres as calibration standards we report that, for flagella-free *E. coli* adhering on a cationic poly-l-lysine (PLL) layer, the cell-surface contact and apparent cell deformation vary with adsorbed cell configuration. Most cells adhere by their ends, achieving small contact areas of 0.15 μm^2, corresponding to about 1-2% of the cell's surface. The altered Gaussian curvatures of end-adhered cells suggests flattening of the envelope within the small contact region. When cells adhere by their sides, the contact area is larger, in the range 0.3-1.1 μm^2 and comprising up to ~12% of the cell's total surface. A region of sharper curvature, greater than that of the cells' original spherocylindrical shape, borders the flat contact region in cases of side-on or end-on cell adhesion, suggesting envelope stress. From the measured curvatures, precise stress distributions over the cell surface could be calculated in future studies that incorporate knowledge of envelope moduli. Overall the small contact areas of end-adhered cells may be a limiting factor for antimicrobial surfaces that kill on contact rather than releasing bactericide.

Keywords: bacteria envelope deformation, cell-surface contact, adhesive bacterial contact area, bacteria envelope stress, membrane, TIRF microscopy

Introduction

In addition to providing a scaffold to support bacterial cells as they grow into biofilms, surfaces direct biofilm formation through physico-chemical interactions with substrate chemistry and through cell adhesion mechanics. Cells can be affected individually, or surface interactions can mediate cell-cell interactions. These behaviors motivate studies of the contact region between cells and surfaces, in real time and under a range of relevant conditions. Such an approach is not broadly possible, however, due to the small size of bacterial cells and the difficulty of probing the contact region.

To explain how cells might respond to interfacial chemistry, current thinking translates mechanisms established for bulk solutions to interfacial environments. For instance, *E. coli* respond to pH changes in solution[1] by upregulating curli and extracellular polysaccharides[2] or by increasing the synthesis of periplasmic proteases to combat pH-driven toxicity[3] while Salmonella, in response to lowered solution pH, alter their lipopolysaccharide compositions in ways associated with antibiotic resistance.[4] It is suggested that the same pathways and genes could be triggered by interfacial pH.[1] Since surfaces typically carry oxide groups, interfacial environments can be quite acidic.[5] Indeed, the nanoscale region where a cell contacts a negatively charged surface is reported to be even more acidic than the interfacial environment further away from adhered cells, a result of cell-substrate interactions.[6] Similarly, cationic surfaces, while in many instances deadly for adhered bacteria, can permit cells to live and propagate if their charge is not too dense.[7, 8] Consequently, cell-surface contact can effect changes in the membrane potential,[9-11] affecting multiple pathways.[12-14] Indeed, strategies for biocidal surfaces rely on the contact between bacterial cells and surfaces presenting cationic

functionality,[7, 8, 15, 16] peptides and peptide-mimicking molecules,[17-20] or functional clusters.[21] Specific adhesive interactions are also responsible for *E. coli* cell rolling in flow.[22-24]

In these examples, the cell's sensitivity to a substrate is expected to depend on the amount of its surface area which resides within nanometers of the substrate. Adhesion-driven cell deformation will increase the contact area and the fraction of the cell experiencing "signal" from a surface. Further, as envelope deformation increases cell-surface contact, geometry requires that at short times when cell volume and area are constant (before there is time for transport and substantial surface restructuring), adhesion-driven cell flattening on rigid surfaces will produce regions of sharp envelope bending, which would experience large mechanical stress. Such mechanical stress could stimulate adhered cells by several other downstream signaling pathways,[1] motivating characterization of near-surface cell shape. Further, adhesive manipulation of envelope shape may enable new killing mechanisms that do not pose chemical hazards.[25]

Beyond the direct impact of surface contact on individual cells, surface chemistry and adhesion can couple with mechanics to direct cell-cell interactions and cell organization in colonies and biofilms.[26] For instance the competition of forces, the attraction of cells to a surface, friction at the surface during growth, and compressive forces from neighboring cells, can produce what resemble snapping or buckling transitions between cell pairs.[27-32] This in turn determines the degree of contact and interaction between neighboring cells as they grow and, in particular the degree of side-to-side contact of cell pairs. These surface-mediated cell-cell interactions and structures in turn govern the transition of the community from a flat two-dimensional collection of cells to a three-dimensional biofilm.[27-31, 33]

These considerations motivate studying the contact region between bacterial cells and surfaces *in-situ,* which is expected to vary greatly with cell configuration, for instance, whether capsular cells adhere by one end or on their sides.[34, 35] AFM studies have provided perspective on the probe-envelope interactions.[36-40] Immobilizing bacterial cells on a cantilever, the interactions between cells and biomaterials have been examined.[41] Yet the timescales (seconds or less) of contact and the contact areas in AFM studies do not reflect the range and more extensive contact which must occur when founder cells initiate biofilms including the minutes or longer timescales relevant to cell division. Gu *et al* have, however, documented cell deformations in early biofilm formation[42] while fluorescence enhancement for *S. aureus* adhering to gold has been employed to track the deformations of collections of cells taken together, providing insight into the dynamics of cell deformation[43] but not the actual surface contact area.

This paper presents a total internal reflectance fluorescence (TIRF) method to probe the nanometric separation distances between an adherent cell and a substrate near the contact region, the extent of cell-surface contact of individual cells, and the shape of the outer bacterial envelope in the contact region, to about 80 nm from the surface. By introducing a small amount of fluorescently-labeled dextran into the solution, a lack of absorption to cells or to the supporting surface allows cells to be visualized as dark spots. Analysis of their fluorescence profiles reveals the shapes of the contact zones with sufficient resolution to provide perspective on bacterial growth and response of cells to the surface environment. We develop this approach using flagella-free *E. coli* strain adhering strongly on a cationic surface where previous work has demonstrated firm cell immobility.[35] We document contact areas and dimensions for cells

adsorbed in different configurations. This study focuses on times less than ~30 minutes. The cells are living and their growth is evident at longer times. The lack of antimicrobial activity of this cationic surface may result from the small contact area, comprising a few percent of the cells' overall surface area.

Experimental Materials and Procedures

Bacterial Cultivation and Characterization. An *E. coli* strain having its flagella protein genetically knocked out, *ΔflhD E. coli* JW1881, was purchased from the Coli Genetic Stock Center (New Haven, CT). Electron microscopy confirmed the lack of flagella and motility plate assays were employed to further confirm a lack of motility.[44, 45]

After growing for 16 h at 37ºC in lysogeny broth (LB) *E. coli* were back-diluted 1:50 in LB, incubated at 37ºC for 2 h, and harvested in log phase. Proteins and other macromolecular constituents in the medium or loosely associated with bacteria were removed by washing, centrifuging, and resuspending the cell suspension three times with phosphate-buffered saline (PBS, 0.008M Na_2HPO_4, 0.002M KH_2PO_4, and 0.15 M NaCl) before finally resuspending in PBS at a concentration of cells 10^8 cells/ml. Each bacterial suspension was used within 1 h of preparation. Viability screening with propidium iodide (Sigma-Aldrich, excitation/emission at 535 nm/ 617 nm) before and after experiments confirmed that the bacteria maintained viability throughout all experimental procedures. Using the Oufti[46] cell detection analysis tool, 100x phase contrast images of the *E. coli* suspensions were analyzed to determine the length and width of each cell. Statistics on cell dimensions were generated for 350 to 400 cells in each of three suspensions grown on separate days. The average cell length was found to be 3.0 ± 0.3 μm and the average cell width was 0.96 ± 0.05 μm. These dimensions are consistent with expectations for *E. coli* in the log phase.[47-49]

Particles. Silica particles were employed as calibration standards. 1 μm silica spheres were purchased from Gel Tech (Orlando) and 2 μm silica spheres were purchased from Bangs Labs.

Fluorescent Agent. FITC-Dextran, 500,000 g/mol (Sigma FD 500S) was employed as the imaging agent to reveal the excluded/depleted region. Concentrations of 1000 ppm, which were employed here, were found to be insufficient to produce measurable depletion aggregation of cells or alter cell adsorption on polycation-coated surfaces. Additional control studies, adding particles or cells to 1000 ppm FITC-Dextran suspension and then sedimenting particles or centrifuging cells revealed no measurable adsorption of fluorescent dextran to the surfaces of cells or particles in fluorescence microscopy images.

Adhesion of Cells or Particles to Surfaces. Fisherfinest cover slips were acid etched overnight, rinsed thoroughly with deionized (DI) water, and sealed in a custom flow chamber having a flow cross section of 0.69 mm x 6.5 mm. The flow of PBS through the chamber was established, and then a 100 ppm solution of Poly-l-lysine (PLL) with nominal molecular weight 15,000-30,000 g/mol from Sigma, was flowed through the chamber at a wall shear rate of 5 s^{-1} for 10 minutes, followed by flowing buffer. This procedure produced an adsorbed polycation layer having a mass of 0.3-0.4 mg/m^2 that rapidly captured and retained cells and or calibration particles. In several other studies[25, 50-52] we established the retention of PLL over a range of ionic strengths and when challenged by adsorbing cells or proteins.

Subsequently, a bacterial suspension, a suspension of silica microspheres, or a mixture of bacteria and microspheres in phosphate buffer was flowed through the chamber, for 20 minutes, followed by buffer flow to remove cells and particles from the suspension. This procedure, conducted with the chamber on its side so the floor of the chamber was oriented parallel to the

lab walls, deposited cells and particles in controllable amounts at their respective transport limited rates. The chamber orientation avoided gravity-driven sedimentation of cells or particles towards or away from on the surface of interest.

Total Internal Reflectance Fluorescence (TIRF) Microscopy. After cells and/or particles were captured on PLL-coated surfaces, the ends of the flow chamber were sealed (stopping any flow) and the chamber was transferred, test surface down, to a Nikon NSTORM TIRF microscope. It was previously established that *E. coli* cells adhering on cationic surfaces such as PLL are immobilized at their areas of contact and are unaffected by moderate shear up to 110 s^{-1}. They neither translate or reorient, within detectible limits,[35] unlike the same cells on glass.[53] The adhered cells were found in a variety of side-on and end-on configurations, the latter at different angles relative to the surface or the flow and within the resolution of the microscope. Since the cells are motionless after their capture on PLL, turning the chamber to fit the microscope is unlikely to alter the established cell-surface contact. Here the chamber was turned within 15 minutes of completion of cell capture. In these studies, cells looking substantially end-on were compared to cells that were substantially tipped down toward the surface, using *E. coli* grown on 3 different days.

In these studies, incident light at the excitation wavelength, λ_o, of the fluorophores is totally internally reflected inside the coverslip to which the cells are adhered. The light impinges the interface from inside the coverslip at incident angle, θ_i relative to the normal, controlled by the TIRF microscope. This produces an evanescent wave of excitation light at the interface between

the functionalized glass and the bacteria suspension. The intensity, I of the evanescent wave decays perpendicular to the coverslip with penetration depth, Λ, according to

$$\Lambda = \frac{\lambda_o}{4\pi\,(n_g^2\,sin\theta_i - n_s^2)^{1/2}} \qquad (1)$$

where n_g and n_s are the refractive indices of the glass coverslip and aqueous solution, respectively.

This paper presents results for an incident angle of 70°corresponding to a penetration depth of Λ= 55.5 nm. Parallel experiments were also run at θ_i = 65° and 75°, corresponding to penetration depths of Λ= 66.2 nm and 49.5 nm, producing quantitatively similar results. TIRF images employed a 100x objective, which yielded a pixel size of 65 nm.

Results and Discussion

Calibrations of Gap Thickness Using Silica Spheres.

1 and 2 μm silica spheres were co-deposited on PLL-coated slides from buffer solutions containing mixtures of 500 and 1000 ppm 1 and 2 μm spheres, respectively. The suspension was flowed past the adhesive slide for 10 seconds, sufficient for particles to be captured sparsely, and then buffer was flowed to remove free particles from the suspension. The captured particles appeared non-aggregated and completely immobilized. Next, 1000 ppm FITC-Dextran in buffer was flowed into the chamber to facilitate fluorescent imaging, and the flow stopped.

Bright field and TIRF images of different fields were obtained at 100x on a Nikon NSTORM TIRF microscope, with incident angles of 65,70, and 75° (measured from the normal) corresponding to evanescent penetration depths of 66.1, 55.5, and 49.5 nm. For the calibration exercise, the analysis focused on fields which contained both 1 and 2 μm particles in proximity, per the example in Figure 1A and 1B shown for Λ = 55.5 nm (70°), so that the same background subtraction could be applied to both particles. The adhered particles appear dark in Figure 1B because the fluorescence comes from the labeled dextran in free solution around the particles. Using ImageJ software, fluorescence was plotted as a function of position along a line drawn through both particles, shown in Figure 1C, a standard correction, for instance employed by Vigeant *et al*.[54] Figure 1D plots the fluorescence profiles measured along two additional lines, parallel to but sufficiently far from the first line to enable background subtraction. The fluorescence profile (along the first line) through the particles was corrected, in Figure 1E, by subtracting the average intensity for each position down the left and right lines from the intensity along the middle line: $I_i = I_i^{init} - \frac{\left(I_i^{left} - I_i^{right}\right)}{2}$.

In the fluorescence profile of Figure 1E, the 2 μm particle makes a wider dark spot than the 1 μm particle. The dark region from either size particle is, however, substantially narrower than the actual particle diameter, a result of the evanescent wave having a smaller decay length than the heights of the particles at their widest points. The evanescent wave samples the interface nearer to the particle-coverslip contact zone. The camera records a substantial background signal beneath the particles, likely the combined effects of dark noise and scattered excitation light, however minimal. The difference in darkness between the two particles is relatively small, and appeared random over a sampling of 20 particles. Due to the finite pixel width of 65 nm, some fluorescence would be expected at the darkest pixel.

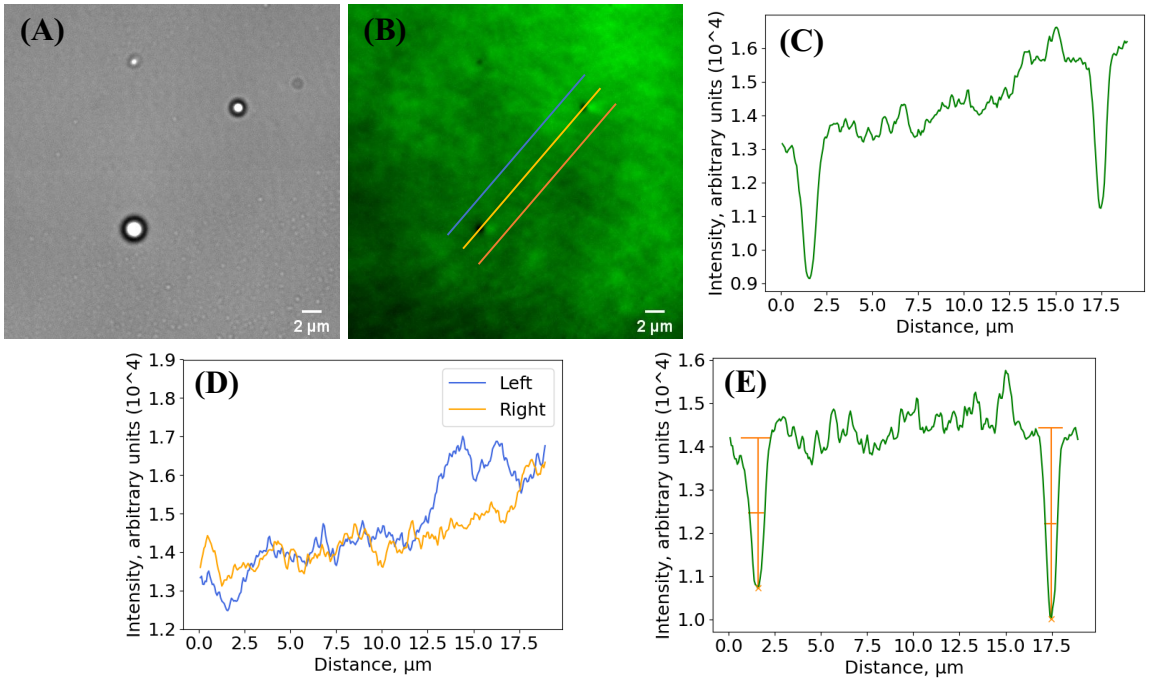

Figure 1. (A) Bright field and (B) TIRF images ($\theta_i = 70°$, $\Lambda = 55.5$ nm) of 2 and 1μm silica spheres, adhered on a PLL-coated flat and immersed in a FITC-Dextran solution. Fluorescence traces along (C) middle and (D) left and right lines indicated in (B). (E) Fluorescence profile after background subtraction of left and right traces from the middle trace.

A calibration was developed to convert from near-particle (or near-bacterium) fluorescence to the local gap height or position-dependent distance between the flat surface and the particle/bacterium, as sketched in Figure 2A. Figures 2B and C for 1 and 2 μm particles, respectively, reveal that the intensity variations for different surface positions (different pixels) within the near-sphere dark regions conform to expectations for the contour of the sphere surface. The expected shape of a sphere-plate contact and the specific values of gap heights up to about 80-100 nm from the surface are found to within a proportionality constant that depends on FITC-dextran concentration and microscope parameters and which must be calibrated. Therefore, in each graph, corrected intensities measured near 10 different particles of each size, in different fields have been averaged. Then the exact calculated shapes of 1 or 2 μm sphere surfaces are superposed, in Figures 2B and C respectively, with the scales for the sphere contours on the right axes. Also shown are shapes of the sphere surfaces plus a 10 nm depletion layer, corresponding to the dextran imaging agent. Further from the center of the sphere where the gap height is larger, the measured fluorescence is less than would be contributed from the entire gap height because the gap height exceeds the evanescent wave depth further from the contact point.

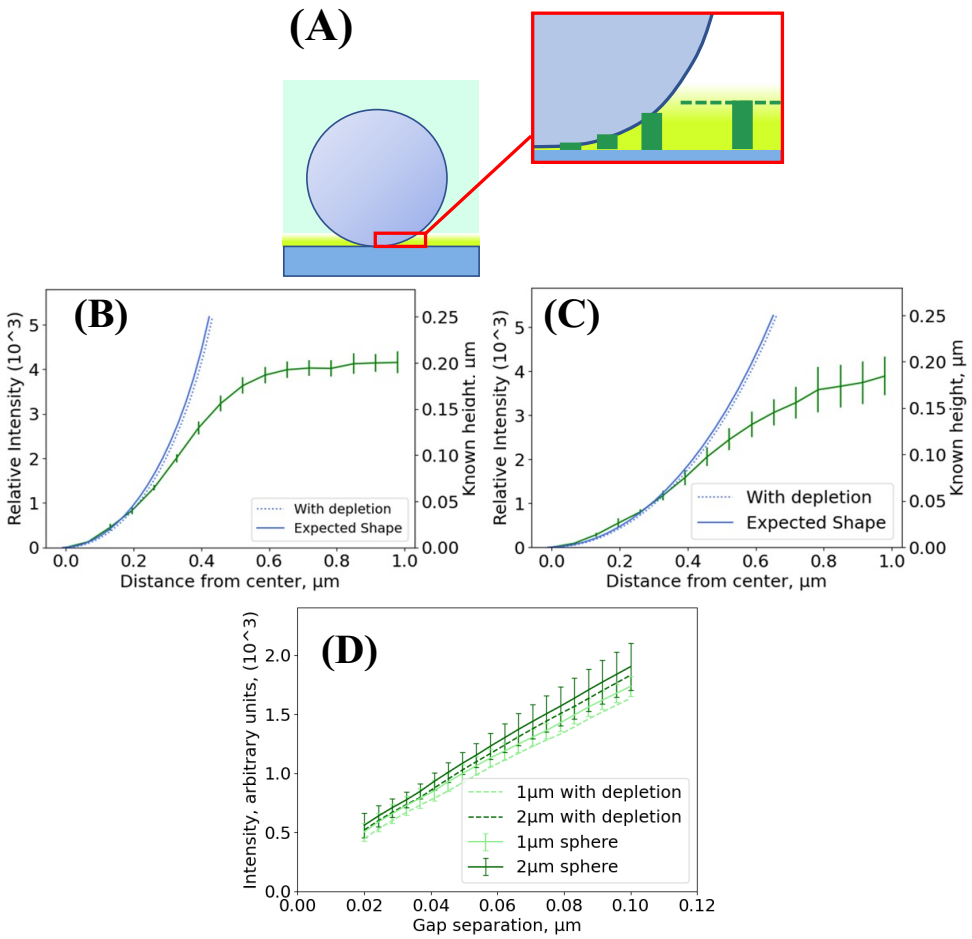

Figure 2. (A) Schematic of gap geometry and the evanescent wave near a sphere. The close up shows 4 green bars representing the fluorescence intensity on different pixels, while the dashed line represents the baseline fluorescence away from contact zone, still beneath sphere. (B) Near-particle fluorescence averaged for 10 different 1 µm spheres and (C) 10 different 2 µm spheres for $\theta_i = 70°$, $\Lambda = 55.5$ nm. In B and C, the shapes of a sphere, or a sphere plus a 10 nm depletion layer are superposed to explore the proportionality between gap height from the sphere shape and the fluorescence intensity. For gap heights larger than ~200 nm, the fluorescence approaches a constant value, determined by the penetration depth of the evanescent field. (D) Calibration curves up to gap heights of 100 nm, showing that 1 µm and 2 µm spheres produce the same calibration constant.

Figure 2D summarizes the proportionality established in Figures 2B and C, suggesting that for gap heights less than the range 80 -100 nm, a single calibration constant relates the measured fluorescence to gap height. The small intercept (extrapolating the data to zero separation) in Figure 2D is a matter of choosing the baseline value for the point of contact or smallest gap. The

calibration curves for 1 μm and 2 μm particles are identical within nanometric experimental error. Similar proportionalities hold, albeit with different calibration constants, at incident angles of 65° and 75°. Small differences in the calibrations using the two different sphere sizes may result from the pixel size of 65 nm, which introduces uncertainty in the "known" gap height as a function of position because the sphere's areas are sloped within each pixel. The gap from the 1 μm sphere varies more sharply than that from the 2 μm sphere within a given pixel. Nonetheless, the similarity of the calibrations in Figure 2D for the two sphere sizes, with uncertainty less than 5 nm for small gaps and less than 10 nm for 100 nm gaps is acceptable in examining contours of near-surface cells. Overall, the resolution is found to be about 10% of the gap height for gaps of 2Λ or less.

Measurements of Spherical Test Particles: Gap heights and Curvatures.

Once the conditions for proportionality between fluorescence and gap height are established, the calibration can be employed to profile a test particle. This exercise is shown in Figures 3 and 4 for calibration spheres chosen to be of a different radii, but in the same frame as the test spherical particles. Figure 3 maps the contour of a 2 μm spherical test particle using a 1 μm calibration sphere. Figure 4 maps the contour of a 1 μm spherical test particle using a 2 μm calibration sphere. Parts A of the two figures show the reconstructed gap heights over the test particle surface within the evanescent field. Also shown in Parts A of both figures are the calculated (exact) shapes of 1 and 2 μm spheres, noting that the differences in x, y, and z scaling exaggerates the vertical scale. From the measured height contours in Part A (blue data) two cross sections, sliced 90° from each other through the center of the test particle, are shown in parts B and C. These sections are compared with the exact spherical contour corresponding to the

nominal size of the test sphere. This exercise reveals that using a sphere of one size to measure a different sphere provides quantification within nanometers of expectations for regions near contact where the gap height is ~2Λ or less.

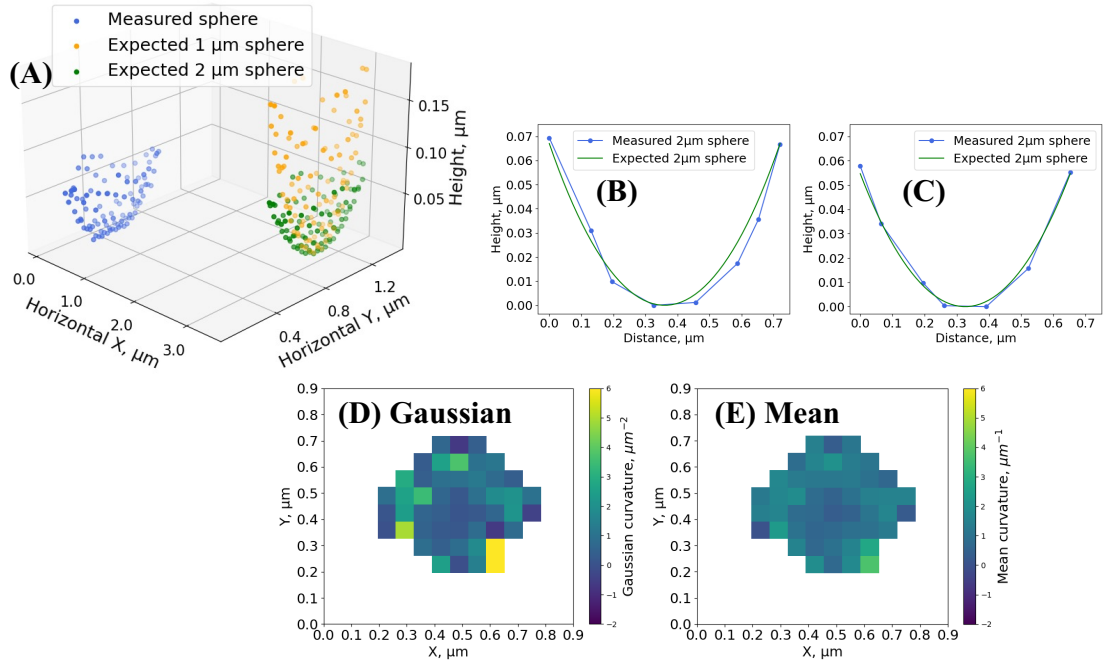

Figure 3. Scan of a typical 2 µm test particle using a 1 µm calibration sphere. (A) Reconstruction of the test particle in blue, with calculated green and orange profiles showing how 1 and 2 µm sphere would look at this scale. (B) and (C) Cross cuts through the reconstructed profile of the 2 µm test particle, sectioned orthogonal to each other and taken approximately the center of the contact region. Heat maps of local (D) Gaussian and (E) mean curvature near the contact region.

Measurements of the gap height for each pixel can be employed to map the local curvature of surfaces in the contact region. The Gaussian curvature K is the product of the curvatures in the two principle (orthogonal) directions: $K = \kappa_1 \kappa_2$. While the Gaussian curvature generally depends on position on a surface, for a sphere of radius r, $K = \frac{1}{r^2}$ everywhere. Likewise along

the sides of a cylinder $K = 0$ everywhere. The mean curvature is defined $H = \frac{\kappa_1+\kappa_2}{2}$ and is exactly $1/r$ everywhere on a sphere and $1/(2r)$ on the sides of a cylinder.

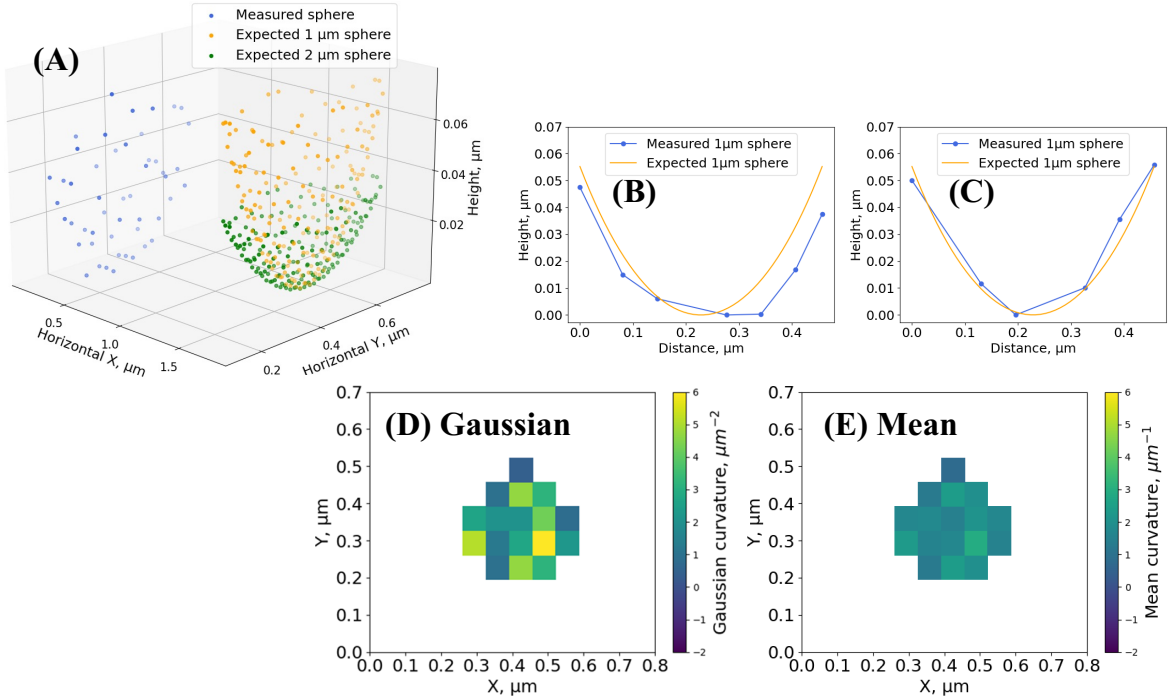

Figure 4. Scan of a typical 1 µm test particle using a 2 µm calibration sphere. (A) Height profiles resulting from the test particle in blue, with calculated green and orange profiles showing how 1 and 2 µm sphere would look at this scale. (B) and (C) Cross cuts through the 3D profile of the 1 µm test particle, sectioned orthogonal to each other and taken approximately the center of the contact region. Heat maps of local (D) Gaussian and (E) mean curvature near the contact region.

The Gaussian and mean curvatures for each pixel of the test spheres in Figures 3 and 4 were calculated starting with the gap height for each pixel, $h(x,y)$, according to:[55]

Gaussian curvature: $$K = \frac{h_{xx}h_{yy}-h_{xy}^2}{(1+h_x^2+h_y^2)^2} \quad (2)$$

Mean curvature: $$H = \frac{(1+h_x^2)h_{yy}+(1+h_y^2)h_{xx}-2h_xh_yh_{xy}}{2(1+h_x^2+h_y^2)^{2/3}} \quad (3)$$

The slopes, h_x, h_y, and second derivates h_{xx}, h_{yy} and hxy were calculated from $h(x,y)$ using numpy.gradient in the Python library.[56]

The results of these curvature calculations are summarized in the heat maps in Figures 3 and 4 parts D and E. The measured Gaussian curvature values for the 2 μm and 1μm test spheres approach the expected values of K = 1 μm^{-2} for the 2 μm sphere and 4 μm^{-2} for the 1 μm sphere. The results are best in the region where the gap is less than 50 nm, becoming noisy further away as the sphere curves up from the surface. Away from the particle's center, the test particle surface is increasingly less parallel to the cover slip, introducing noise into the data. Additional spheres, ten of each size, were imaged and analyzed by this method. For ten 1μm-diameter test spheres, an average Gaussian curvature of K=4.2 μm^{-2} and an average mean curvature of H = 2.3 μm^{-1} was measured. For ten 2 μm-diameter test spheres, an average Gaussian curvature of K=1.4 μm^{-2} and an average mean curvature of H = 1.4 μm^{-1} was measured. These results are highly encouraging because 1) the spherical character of the test particles is apparent in the constant curvature values and symmetry of the mapped regions and 2) the measured and expected values are in good agreement. Since the analysis requires calculation of second derivatives of experimental data, one might expect far worse. Especially in the case of Gaussian curvature calculations, multiplication of second derivatives in the principal directions magnifies error, yet the results are quite reasonable, confirming the nominal sphere sizes from the manufacturers.

Based on the ability to resolve the known shapes and curvatures of spherical microparticles, which establishes the method of calibration, we applied this approach to *E. coli* cells in the analysis below. The success of the method for anionic particles adhering to a cationic surface suggests that the measured fluorescence is dominated by labels on free chains and that any

adsorption of the dextran to the cationic PLL surface or the negative microparticles is too small to impact the proportionality between fluorescence signal and gap thickness.

Gap Height and Envelope Curvature in the Contact Region near Adhered Bacteria.

The microsphere-based calibration for gap height was applied to examine the extent of contact and shape of the contact region of *E. coli* cells captured on cationic PLL surfaces. The cells, present at a concentration of 10^8 cells / ml in a buffered suspension that also contained a small amount of calibration microspheres (250 ppm of 1 μm microspheres and 500 ppm of 2 μm microspheres), were captured on a PLL-functionalized glass cover from gentle shear flow. The lateral orientation of the flow chamber avoided gravitational settling of cells towards or away from the surface during capture. After sufficient cells were captured, buffer was replaced by flowing FITC dextran. The then the pump was shut off, the tubing sealed, and the chamber transferred to the TIRF microscope.

Prior work demonstrated that *E. coli* are captured in a variety of configurations, for instance standing on-end mostly perpendicular the surface, or leaning toward the surface, or appearing tipped over and possibly in full side-on contact.[35] The current study examined 8-10 cells in each of two cell configurations, standing versus tipped (or side-adhered), on 3 cationic PLL-functionalized surfaces prepared separately. It is important to note that in contrast to the adhesion of *E. coli* on glass surfaces where cells can wiggle or reorient reversibly in flow,[35, 53] on cationic surfaces the cells are fixed in place and do not move or reorient when flow is stopped or increased to a wall shear rate of 110 s^{-1} or greater. This makes it likely that when the chamber

was turned to fit the TIRF microscope the cells remained fixed and do not reorient on the surface.

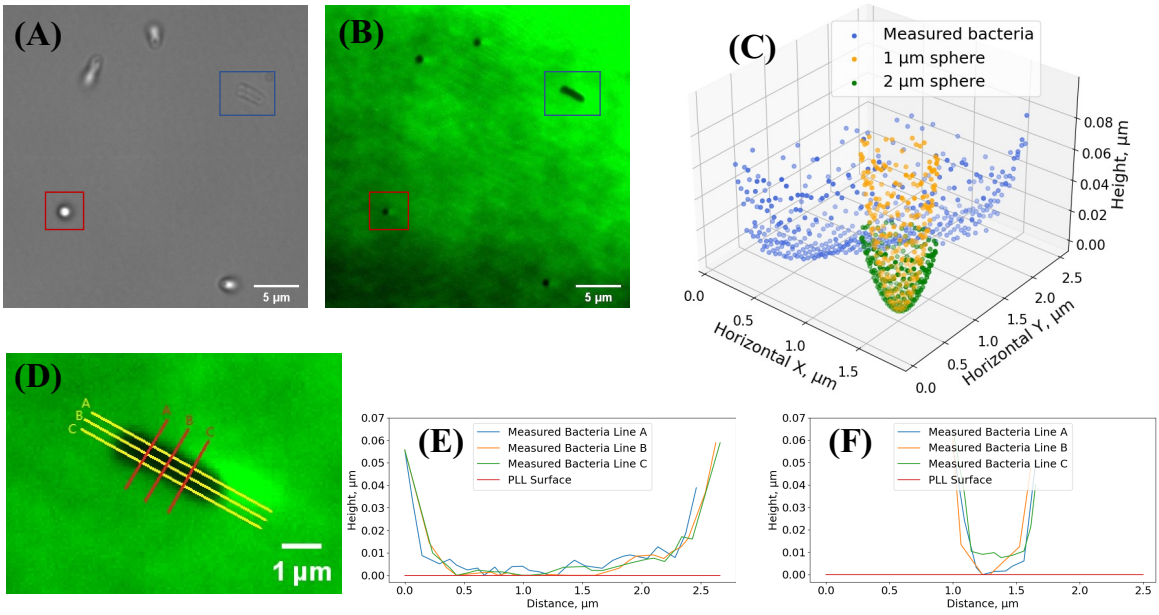

Figure 5. (A) Bright field and (B) TIRF images of a field containing 3 cells and two 1 µm spheres. The cell that is analyzed is boxed blue and the spherical calibration particle is boxed red. (C) Reconstructed profile of bacterial cell, superposed with the calculated height profiles of a 2µm (green) and 1µm (orange) sphere, for perspective. D). Closeup of fluorescent image showing lines along which gap separations are shown in E, and F. (E) Three long-way sections through the adhered bacterium. (F) Three cross sections through the adhered bacterium. A lack of phase contrast can make side-adhered cells, arranged flat to the surface like that in the blue box of Figure 5A, difficult to see.

Figures 5 and 6 show example data and analysis for two cells, one tipped in a side-on configuration and the other in a vertical standing orientation, respectively. Parts A and B of each figure show bright field and fluorescence images where microspheres and bacteria appear dark because they exclude the fluorescent dextran. Part C shows the gap height reconstruction as a function of position, resulting from a microsphere-based calibration described in the previous section. Part C superposes the exact shapes of 1 µm and 2 µm spheres for reference. The side-adhered cell in Figure 5 appears as a dark elongated shape while the end-adhered cell in Figure 6 and others in Figure 5 appears as dark circles as do the calibration beads. The beads and end-on

cells are distinguishable in bright field because, focusing upwards from the cover slip, the calibration spheres disappear from focus while the protrusion and cylindrical character of the end-on cells is evidenced by a circular cross section that remains in focus 2-3 μm above the focal plane of the flat surface.

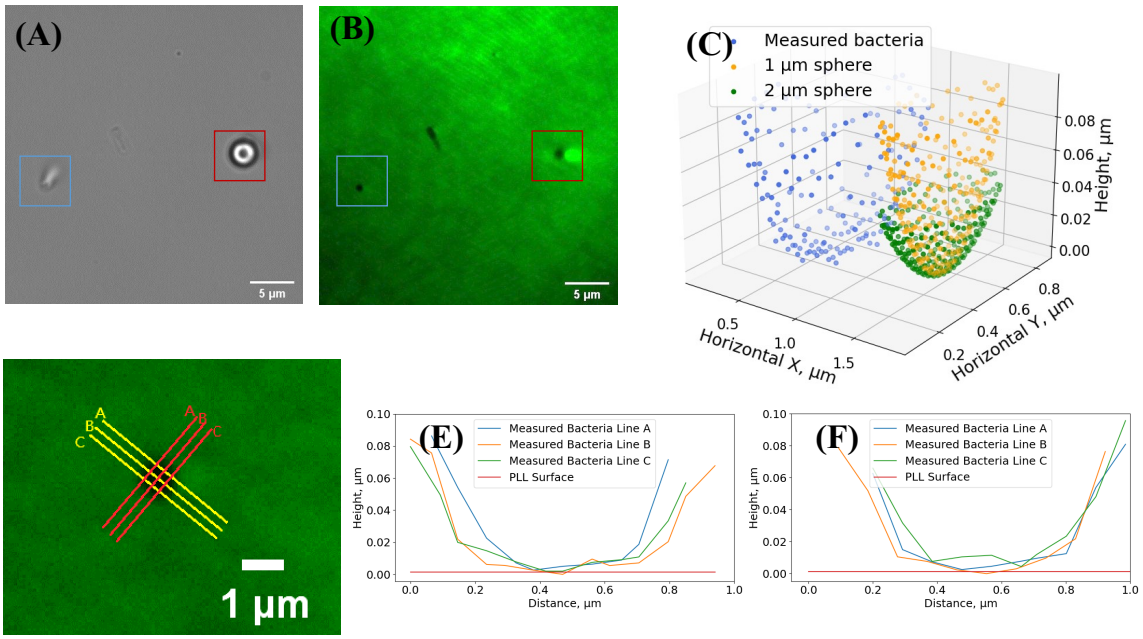

Figure 6. (A) Bright field and (B) TIRF images of field containing 2 cells and a 2 μm calibration sphere. The cell that is analyzed is boxed blue and the spherical calibration particle is boxed red. (C) Reconstructed profile of bacterial cell superposed with calculated height profiles of a 2μm (green) and 1μm (orange) sphere, for perspective. D). Closeup of fluorescent image of the cell, showing lines along which gap separations are shown in E, and F. (E) and (F) Sections through the adhered bacterium corresponding to the yellow and red cuts in D, respectively.

The gap height reconstructions of the contact regions in Parts C of Figures 5 and 6 summarize the bacteria-surface separation as a function of position while parts D-F show select cross-

sections. Because a fluorescent depletant is employed, the gap represents the contour of the outside of the bacterial envelope. In the case of the side-on cell in Figure 5, an elongated contact region is evident in the 3D plot and the individual cross sections.

The smallest gap thickness, defining the nature of contact, is very sensitive the choice of baseline, as discussed in the description of the calibration. We chose the baseline conservatively, so that the darkest pixel defined the zero gap height. This approach, influenced by noise in the fluorescence signal, gives the largest gap thicknesses (order 5 nm) in much of the contact region, while we believe the gap may actually be narrower. Alternately, one could choose the darkest region of the contact zone and average the intensities in that area to define the height corresponding to zero nanometers. This approach, which we did not employ, can allow some pixels to have negative gap heights, by 2-3 nm, though it might more accurately describe other parts of the contact zone. The issue arises because individual pixels may contain regions where the cell is in contact with the surface and other regions where there is nanometric gap, making perfect contact hard to identify.

Despite the challenge of identifying perfect contact, there appears to be a contact or near-contact zone, an extensive region measuring 1.3 μm long and 0.3 μm wide, for the cell in Figure 5, where the cell is less than a maximum of 5 nm from the surface and beyond which the cell-surface gap increases. (The contact region has dimensions of 2.3 μm long and 0.4 μm wide if a 10 nm gap height, a maximum estimate, is chosen as the threshold). The sharp increase in gap height beyond the contact region grows by 45 nm in a single pixel of 65 nm size along much of the contact perimeter. While we typically think of a 10 nm gap as a relatively large separation

and lacking true contact, it may be a substantial overestimate based on baseline fluorescence noise. The appearance of the cell in Figure 5D-F suggests substantial substrate-cell interactions, manifest in a flat middle region a sharper curvature beyond the region of <10 nm gap height. Even within this region of close-cell surface interaction it should be noted that the middle longways crosscutting line exhibits a zero gap height for a distance of ~1.2 μm over the length of this ~3 μm cell. The example end-adsorbed cell of Figure 6 exhibits an expected small contact area with the surface. Slight differences between the bacterium ends and a spherical shape are evident. There is also a difference in the shapes of the rounder cross sections of the end-adhered cells (Figures 6E and F) and the across-cut profiles of the side-adhered cell (Figures 5E and F) where the latter appear slightly flatter.

Beyond noting the flat-looking contact region and sharp increase in cell-surface separation beyond the contact zone, it is possible to quantify the local Gaussian and mean curvatures of the outer envelope, summarized in Figure 7 for the example side on and end-on cells from Figures 5 and 6. Employing equations 2 and 3 reveals position-dependent curvature on the bacteria cell surface, distinct from the expected nearly constant curvature of the calibration particles.

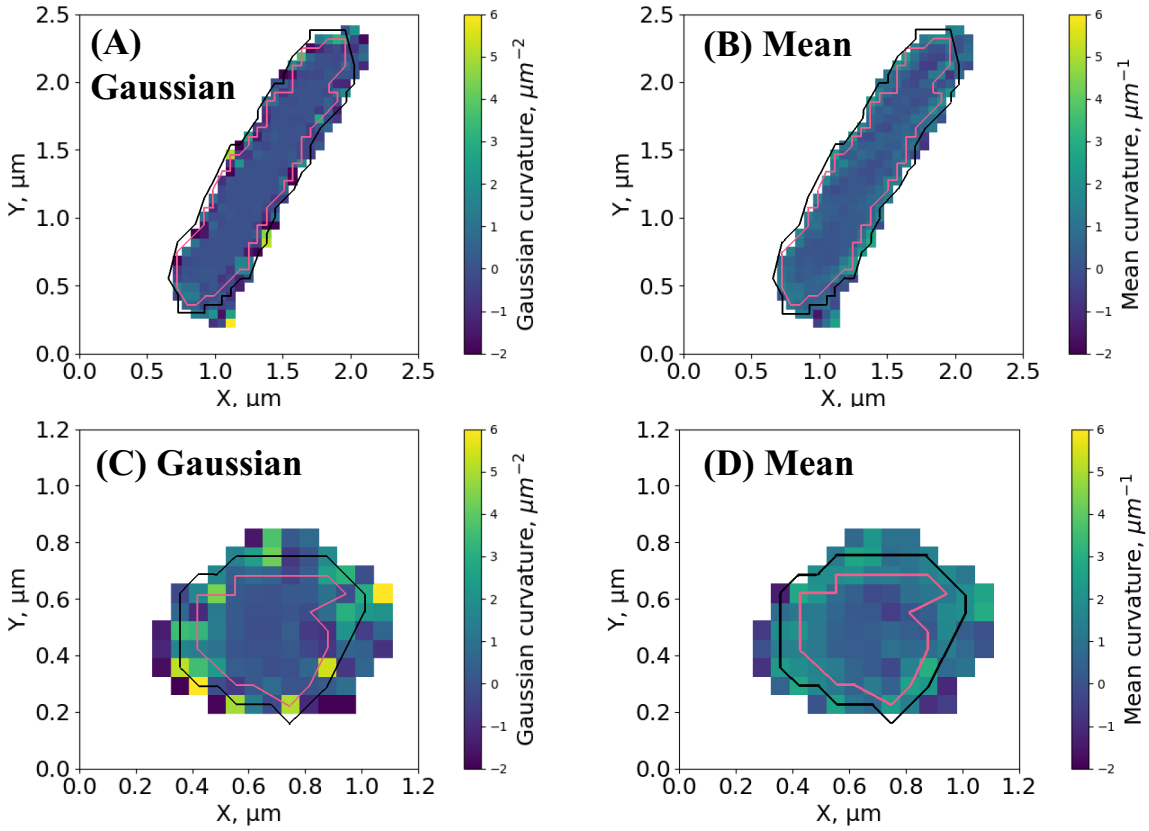

Figure 7. Gaussian (A and C) and mean (B and D) curvatures for the same side-adhered (A) and (B) and end-adhered (C) and (D) cells in the examples of Figures 5 and 6. The red and black curves) are topography lines indicating the bounds for gap heights of 10 and 20 nm respectively. A version without these lines is available in the Supporting Information.

The near-zero Gaussian curvature in the contact zone and along the sides of the side-adhered cell in Figure 7A suggests a cylindrical or flat shape, but cannot distinguish between the two. However in the same region in Figure7B, mean curvature values between 0 and 0.5 μm^{-1} fall below the expected value of 1 μm^{-1} for a 1 µm diameter cylinder, suggesting that this part of the cell is flat or nearly so. These results are consistent with the cell's appearance in Figure 5E and F but are quantified here. At the periphery of the flat zone the mean curvature jumps to values between 2-3 μm^{-1} indicating sharper bending of the cell envelope. Towards the ends of the side-adhered cell, the Gaussian curvature increases, reflecting the curvature of its spherical caps.

Topography lines are superposed with the curvature heat maps, demonstrating that, at contact and for gaps nanometrically greater than tight contact, the cells are substantially deformed from their presumed initial spherocylindrical shapes. The Supporting Information contains the same curvature heat maps without the topography lines, to facilitate closer viewing.

For the end-adhered example, the cell exhibits flatness at its adhered end, with a Gaussian curvature near 1 μm^{-2} in Figure 7C, in sharp contrast to expectations for the Gaussian curvature of an undeformed 1 μm diameter sphere ($K = 4\ \mu m^{-2}$) in Figure 4D. Beyond the flat central regions in Figure 7C and D, a ring of sharper curvature at the edge of the contact region suggests additional cell deformation.

The dimensions and areas of the contact zones are summarized in Table 1 for cells observed on three different PLL-coated surfaces, adsorbed in side-on and end-on configurations. (Curvature data were obtained for all cells but are difficult to tabulate because of the spatially varying character of these data and their additional cell-cell variations, which might be expected.)

Table 1: Dimensions and Areas of Contact Zones

	Contact Area, μm^2, TH= 20 nm* , (range)	Contact Area, μm^2, TH= 10 nm* (range)	Contact Length, μm (range)	Contact Width, μm (range)
Side-on (13 cells)	0.67 ± 0.26 (0.32 – 1.1)	0.50 ± 0.24 (0.24 – 1.0)	1.71± 0.56 (2.7 – 1.1)	0.53 ± 0.16 (0.25 – 0.9)
End-on (14 cells)	0.21 ± 0.09 (0.06 – 0.43)	0.15 ± 0.08 (0.04 – 0.19)	NA	NA

*TH indicates the threshold distance from the surface in estimating the contact area. A TH of 10 nm was used in estimating lengths and widths of the contact zone.

Implications for Contact Shape and Area.

Visualizing the near-substrate contact region of *E. coli* cells revealed the shapes of the outer surfaces of their cell envelopes and the shapes and areas of the contact zones on a strongly adhesive cationic substrate. The resolution was about 10%, down to a few nanometers at contact. The gap in the contact region for bacteria carried uncertainty of a nanometers due to baseline noise. It was demonstrated that micro-spherical shapes could be quantified with adequate nanometric precision, distinct from other shapes. The region of adhesive interaction between *E. coli* cells and a cationic substrate was shown to be characterized by a flat envelope within the adhesive or contact zone, and envelope bending at the periphery of the contact zone. It was observed that the bending at the zone's periphery was sharper than the undeformed local Gaussian or mean curvatures of a spherocylinder. Comparison of the distinctly different contact zones of microparticles and *E. coli* bacteria established that the outer envelope shape could be measured within the precision of a few nanometers even if the absolute gap height near contact could not be resolved better than 2-3 nm.

The data of Table 1 make clear that the contact areas of *E. coli* cells on oppositely charged rigid substrates are small, about 0.15 μm^2 for cells adhered by their ends in a somewhat vertical configuration, and in the range of 0.3-1.1 μm^2 for cells that are tipped towards the surface. Substantial irregularities and variations in the lengths of the contact of tipped cells are the reasons for the variation. The adhesive contact areas constitute a small fraction of a cells' overall surface area. For instance, treating a cell as a 3.0 μm long spherocylinder with a radius of 0.48 μm (the average dimensions measured in characterization), the total surface area is 9.05 μm^2. Standing cells, with a 0.2 μm^2 adhesive contact have only 2% of their exterior surface in contact with the cationic substrate. A slightly larger area fraction, no more than 10% for tipped

side-adhered cells, might be within range of electrostatic interactions with the surface at low ionic strengths. Therefore in general, but especially at salty conditions such as those with a 1 nm Debye length, electrostatic interactions with cationic substrates are limited. This is important because, for instance, it presents a challenge for cationic and other surface designs that kill cells on contact.

Another consequence of the small contact areas of adherent *E. coli* cells on cationic surfaces is the high areal concentration of adhesive stress. We previously calculated the torques and forces on end-adhered *E. coli* cells in shearing flow, which depend on the angle of the adhered cells and are greatest for cells in an entirely vertical configuration.[35] Integrating the hydrodynamic force from a shear rate of 110 s^{-1} along the entire 3 μm length of a vertically oriented cell reveals a maximum torque of 6.1 x 10^{-12} g cm^2/s^2 and, in the direction parallel to the surface, a force of 3 x10^{-8} g cm/s^2 or 0.3 pN. For end-adhered cells with a contact area of 0.15 μm^2, which stand rigidly in shear at wall shear rate of 110s^{-1}, this translates to an interfacial shear stress exceeding 2 Pa. While this seems like a small number, it is interesting to note that neutrophils, interacting with selectins, dislodge from surfaces at an order of magnitude lower stress[57] and roll at stresses of 0.5 Pa on surfaces that are dense with e-selectins.[58] These dynamic processes with mammalian cells involve much larger contact areas due to the 10 μm scale of the white blood cells and the cell softness, implying stronger interactions for the bacterial cells on these cationic surfaces. It is important to note that cells captured in this study are alive and undergo cell division on timescales longer than the measurements shown here.

Integration of measured curvatures and in-plane strain with measurements and models for envelope and membrane moduli will enable an understanding of local and global stress states of

bacterial cells, for instance possibly opening membrane pores.[59] Current thinking is that the peptidoglycan layer of *E. coli*, on its own, is less stiff than either the inner or outer membranes which individually can have bending moduli on the order of tens of k_BT.[60] Bending stiffnesses of the composite structures are enhanced by the connections between layers; however in some conditions, the stiffness of the outer *E. coli* membrane is load bearing[61] and dominates mechano-sensing, increasing the relevance of the current report on the exterior shape of *E. coli*. adhering on cationic surfaces.

Conclusions

This work demonstrated how small amounts of fluorescent dextran in free solution can be exploited in the Total Internal Reflectance Fluorescence imaging of adherent bacterial cells to reveal their surface contact areas and envelope shapes near a rigid substrate. This experimental approach resolved gap heights normal to the substrate in the contact region to within 10% error, down to ~3 nanometers, but lateral resolution was limited by the microscope magnification and pixel size. In addition to quantifying the effective contact area, the method distinguished the shapes of rigid 1 and 2 μm spherical microparticles in the region of contact up to gap heights of ~80 nm, about twice the pentation depth of the evanescent wave. The shapes of deformable adherent *E. coli* in the first ~80 nm from the substrate were qualitatively and quantitatively distinct from those of adhered rigid microparticles. Indeed, while the studies in this work employed flagella-free *E. coli*, the successful mapping of microsphere surfaces suggests the approach could be extended to cocci such as *Staphylococcus aureus*.

E. coli adhering to a cationic surface, glass coated with PLL, were chosen as the model system for this work because *E. coli* were previously established to adhere firmly, without perturbation

by flow, while remaining viable. The lack of discernable cell motion or reorientation rendered cells easy to image and provided meaningful traces of the contact regions. The contact areas and envelope shapes of *E. coli* adhered on cationic PLL surfaces were strongly dependent on the adhered cell-configuration: side-on or end-on. For end-on cells, an average contact area of 0.15 μm^2 was found, with flattening of the cell envelope in the contact region and sharper bending of the envelope at the periphery of the contact zone. For cells appearing in a side-on configuration, the contact region varied in length due to small differences in the angle at which the cell was trapped, producing contact areas in the range 0.3 – 0.9 μm^2. Flattening of the contact zone and sharper bending towards its periphery was evident in the observed values of the mean curvature, while elevated mean and Gaussian curvatures towards the poles were consistent the cells' spherocylindrical shape.

The small contact areas, comprising only ~2% of the surface area of cells adhered in an end-on configuration, suggest challenges in creating surfaces that kill cells on contact. At the same time, the fact functionalized surfaces can act as effective biocidal materials, combined with the established sensitivity of adhered *E. coli* to the interfacial environment, provide evidence for the extreme responsiveness of *E. coli* to their chemical and mechanical environments, motivating future work on using chemical and mechanical cues to manipulate bacterial cells and biofilms.

Supporting Information. Gaussian and Mean Curvatures Measured for the Example cells of Figure 7

Acknowledgements. This work was supported by NSF1848065. M.N. Smith acknowledges partial support from an NIH traineeship, the Biotechnology Program Fellowship, T32 GM135096. We are grateful to R. Gordon and S. Rivera of the Siegrist Lab for growing bacteria and measuring their dimensions.

References

1. Kimkes, T. E. P.; Heinemann, M. How Bacteria Recognise and Respond to Surface Contact FEMS Microbiol. Rev. 2020, 44, 106-122.

2. Ogasawara, H.; Yamamoto, K.; Ishihama, A. Role of the Biofilm Master Regulator Csgd in Cross-Regulation between Biofilm Formation and Flagellar Synthesis Journal of Bacteriology 2011, 193, 2587-2597.

3. Danese, P. N.; Silhavy, T. J. Cpxp, a Stress-Combative Member of the Cpx Regulon Journal of Bacteriology 1998, 180, 831-839.

4. Perez, J. C.; Groisman, E. A. Acid Ph Activation of the Pmra/Pmrb Two-Component Regulatory System of Salmonella Enterica Molecular Microbiology 2007, 63, 283-293.

5. Russel, W. B.; Saville, D. A.; Schowalter, W. R., *Colloidal Dispersions*. Cambridge University Press: Cambridge, 1989.

6. Ponsonnet, L.; Boureanu, M.; Jaffrezic, N.; Othmane, A.; Dorel, C.; Lejeune, P. Local Ph Variation as an Initial Step in Bacterial Surface-Sensing and Biofilm Formation Materials Science & Engineering C-Biomimetic and Supramolecular Systems 2008, 28, 896-900.

7. Murata, H.; Koepsel, R. R.; Matyjaszewski, K.; Russell, A. J. Permanent, Non-Leaching Antibacterial Surfaces - 2: How High Density Cationic Surfaces Kill Bacterial Cells Biomaterials 2007, 28, 4870-4879.

8. Kugler, R.; Bouloussa, O.; Rondelez, F. Evidence of a Charge-Density Threshold for Optimum Efficiency of Biocidal Cationic Surfaces Microbiology-Sgm 2005, 151, 1341-1348.

9. Brown, D. G.; Hong, Y. Impact of the Charge-Regulated Nature of the Bacterial Cell Surface on the Activity of Adhered Cells Journal of Adhesion Science and Technology 2011, 25, 2199-2218.

10. Raafat, D.; von Bargen, K.; Haas, A.; Sahl, H. G. Insights into the Mode of Action of Chitosan as an Antibacterial Compound Applied and Environmental Microbiology 2008, 74, 3764-3773.

11. Yang, Y.; Zhu, H. G.; Colvin, V. L.; Alvarez, P. J. Cellular and Transcriptional Response of Pseudomonas Stutzeri to Quantum Dots under Aerobic and Denitrifying Conditions Environmental Science & Technology 2011, 45, 4988-4994.

12. Shabala, L.; Bowman, J.; Brown, J.; Ross, T.; McMeekin, T.; Shabala, S. Ion Transport and Osmotic Adjustment in Escherichia Coli in Response to Ionic and Non-Ionic Osmotica Environmental Microbiology 2009, 11, 137-148.

13. Belas, R. Biofilms, Flagella, and Mechanosensing of Surfaces by Bacteria Trends in Microbiology 2014, 22, 517-527.

14. Ashok, N.; Bauer, C. E. Evidence of Defined Temporal Expression Patterns That Lead a Gram-Negative Cell out of Dormancy Plos Genetics 2020, 16, 1008660.

15. Madkour, A. E.; Dabkowski, J. A.; Nusslein, K.; Tew, G. N. Fast Disinfecting Antimicrobial Surfaces Langmuir 2009, 25, 1060-1067.

16. Barbosa, M.; Costa, F.; Monteiro, C.; Duarte, F.; Martins, M. C. L.; Gomes, P. Antimicrobial Coatings Prepared from Dhvar-5-Click-Grafted Chitosan Powders Acta Biomaterialia 2019, 84, 242-256.

17. Kazemzadeh-Narbat, M.; Cheng, H.; Chabok, R.; Alvarez, M. M.; De La Fuente-Nunez, C.; Phillips, K. S.; Khademhosseini, A. Strategies for Antimicrobial Peptide Coatings on Medical Devices: A Review and Regulatory Science Perspective Critical Reviews in Biotechnology 2021, 41, 94-120.

18. Santos, C. M.; Kumar, A.; Kolar, S. S.; Contreras-Caceres, R.; McDermott, A.; Cai, C. Z. Immobilization of Antimicrobial Peptide Ig-25 onto Fluoropolymers Via Fluorous Interactions and Click Chemistry Acs Applied Materials & Interfaces 2013, 5, 12789-12793.

19. Sun, H.; Hong, Y. X.; Xi, Y. J.; Zou, Y. J.; Gao, J. Y.; Du, J. Z. Synthesis, Self-Assembly, and Biomedical Applications of Antimicrobial Peptide-Polymer Conjugates Biomacromolecules 2018, 19, 1701-1720.

20. Zhang, Z. J.; Kou, N.; Ye, W. L.; Wang, S.; Lu, J. J.; Lu, Y.; Liu, H. Y.; Wang, X. M. Construction and Characterizations of Antibacterial Surfaces Based on Self-Assembled Monolayer of Antimicrobial Peptides (Pac-525) Derivatives on Gold Coatings 2021, 11, 1014.

21. Fang, B.; Jiang, Y.; Nusslein, K.; Rotello, V. M.; Santore, M. M. Antimicrobial Surfaces Containing Cationic Nanoparticles: How Immobilized, Clustered, and Protruding Cationic Charge Presentation Affects Killing Activity and Kinetics Colloids and Surfaces B-Biointerfaces 2015, 125, 255-263.

22. Thomas, W., Catch Bonds in Adhesion. In *Annual Review of Biomedical Engineering*, 2008; Vol. 10, pp 39-57.

23. Thomas, W. E.; Nilsson, L. M.; Forero, M.; Sokurenko, E. V.; Vogel, V. Shear-Dependent 'Stick-and-Roll' Adhesion of Type 1 Fimbriated Escherichia Coli Molecular Microbiology 2004, 53, 1545-1557.

24. Thomas, W. E.; Trintchina, E.; Forero, M.; Vogel, V.; Sokurenko, E. V. Bacterial Adhesion to Target Cells Enhanced by Shear Force Cell 2002, 109, 913-923.

25. Fang, B.; Jiang, Y.; Rotello, V. M.; Nusslein, K.; Santore, M. M. Easy Come Easy Go: Surfaces Containing Immobilized Nanoparticles or Isolated Polycation Chains Facilitate Removal of Captured Staphylococcus Aureus by Retarding Bacterial Bond Maturation Acs Nano 2014, 8, 1180-1190.

26. Dalton, H. M.; Poulsen, L. K.; Halasz, P.; Angles, M. L.; Goodman, A. E.; Marshall, K. C. Substratum-Induced Morphological Changes in a Marine Bacterium and Their Relevance to Biofilm Structure Journal of Bacteriology 1994, 176, 6900-6906.

27. Duvernoy, M. C.; Mora, T.; Ardre, M.; Croquette, V.; Bensimon, D.; Quilliet, C.; Ghigo, J. M.; Balland, M.; Beloin, C.; Lecuyer, S.; Desprat, N. Asymmetric Adhesion of Rod-Shaped Bacteria Controls Microcolony Morphogenesis Nature Communications 2018, 9, 1120.

28. Mamou, G.; Mohan, G. B. M.; Rouvinski, A.; Rosenberg, A.; Ben-Yehuda, S. Early Developmental Program Shapes Colony Morphology in Bacteria Cell Reports 2016, 14, 1850-1857.

29. Beroz, F.; Yan, J.; Meir, Y.; Sabass, B.; Stone, H. A.; Bassler, B. L.; Wingreen, N. S. Verticalization of Bacterial Biofilms Nat. Phys. 2018, 14, 954-+.

30. Nijjer, J.; Li, C. H.; Zhang, Q. T.; Lu, H. R.; Zhang, S. L.; Yan, J. Mechanical Forces Drive a Reorientation Cascade Leading to Biofilm Self-Patterning Nature Communications 2021, 12, 6632.

31. Zhang, Q. T.; Li, J.; Nijjer, J.; Lu, H. R.; Kothari, M.; Alert, R.; Cohen, T.; Yan, J. Morphogenesis and Cell Ordering in Confined Bacterial Biofilms Proc. Natl. Acad. Sci. U. S. A. 2021, 118, 2107107118.

32. Liu, Y.; Li, B.; Feng, X. Q. Buckling of Growing Bacterial Chains Journal of the Mechanics and Physics of Solids 2020, 145, 104146.

33. Fei, C. Y.; Mao, S.; Yan, J.; Alert, R.; Stone, H. A.; Bassler, B. L.; Wingreen, N. S.; Kosmrlj, A. Nonuniform Growth and Surface Friction Determine Bacterial Biofilm Morphology on Soft Substrates Proc. Natl. Acad. Sci. U. S. A. 2020, 117, 7622-7632.

34. Jones, J. F.; Feick, J. D.; Imoudu, D.; Chukwumah, N.; Vigeant, M.; Velegol, D. Oriented Adhesion of Escherichia Coli to Polystyrene Particles Applied and Environmental Microbiology 2003, 69, 6515-6519.

35. Xu, Z.; Niu, W. A.; Rivera, S. L.; Tuominen, M. T.; Siegrist, M. S.; Santore, M. M. Surface Chemistry Guides the Orientations of Adhering E. Coli Cells Captured from Flow Langmuir 2021, 37, 7720-7729.

36. Fang, H. H. P.; Chan, K. Y.; Xu, L. C. Quantification of Bacterial Adhesion Forces Using Atomic Force Microscopy (Afm) Journal of Microbiological Methods 2000, 40, 89-97.

37. Dupres, V.; Menozzi, F. D.; Locht, C.; Clare, B. H.; Abbott, N. L.; Cuenot, S.; Bompard, C.; Raze, D.; Dufrene, Y. F. Nanoscale Mapping and Functional Analysis of Individual Adhesins on Living Bacteria Nature Methods 2005, 2, 515-520.

38. Amro, N. A.; Kotra, L. P.; Wadu-Mesthrige, K.; Bulychev, A.; Mobashery, S.; Liu, G. Y. High-Resolution Atomic Force Microscopy Studies of the Escherichia Coli Outer Membrane: Structural Basis for Permeability Langmuir 2000, 16, 2789-2796.

39. Camesano, T. A.; Abu-Lail, N. I. Heterogeneity in Bacterial Surface Polysaccharides, Probed on a Single-Molecule Basis Biomacromolecules 2002, 3, 661-667.

40. Camesano, T. A.; Logan, B. E. Probing Bacterial Electrosteric Interactions Using Atomic Force Microscopy Environmental Science & Technology 2000, 34, 3354-3362.

41. Ong, Y. L.; Razatos, A.; Georgiou, G.; Sharma, M. M. Adhesion Forces between E-Coli Bacteria and Biomaterial Surfaces Langmuir 1999, 15, 2719-2725.

42. Gu, J. H.; Valdevit, A.; Chou, T. M.; Libera, M. Substrate Effects on Cell-Envelope Deformation During Early-Stage Staphylococcus Aureus Biofilm Formation Soft Matter 2017, 13, 2967-2976.

43. Carniello, V.; Peterson, B. W.; Sjollema, J.; Busscher, H. J.; van der Mei, H. C. Surface Enhanced Fluorescence and Nanoscopic Cell Wall Deformation in Adhering Staphylococcus Aureus Upon Exposure to Cell Wall Active and Non-Active Antibiotics Nanoscale 2018, 10, 11123-11133.

44. Shave, M. K.; Santore, M. M. Motility Increases the Numbers and Durations of Cell-Surface Engagements for Escherichia Coli Flowing near Poly(Ethylene Glycol)-Functionalized Surfaces Acs Applied Materials & Interfaces 2022, 14, 34342-34353.

45. Shave, M. K.; Xu, Z.; Raman, V.; Kalasin, S.; Tuominen, M. T.; Forbes, N. S.; Santore, M. M. Escherichia Coli Swimming Back toward Stiffer Polyetheylene Glycol Coatings, Increasing Contact in Flow Acs Applied Materials & Interfaces 2021, 13, 17196-17206.

46. Paintdakhi, A.; Parry, B.; Campos, M.; Irnov, I.; Elf, J.; Surovtsev, I.; Jacobs-Wagner, C. Oufti: An Integrated Software Package for High-Accuracy, High-Throughput Quantitative Microscopy Analysis Molecular Microbiology 2016, 99, 767-777.

47. Harris, L. K.; Theriot, J. A. Relative Rates of Surface and Volume Synthesis Set Bacterial Cell Size Cell 2016, 165, 1479-1492.

48. Hashimoto, M.; Ichimura, T.; Mizoguchi, H.; Tanaka, K.; Fujimitsu, K.; Keyamura, K.; Ote, T.; Yamakawa, T.; Yamazaki, Y.; Mori, H.; Katayama, T.; Kato, J. Cell Size and Nucleoid Organization of Engineered Escherichia Coli Cells with a Reduced Genome Molecular Microbiology 2005, 55, 137-149.

49. Young, K. D., Bacterial Shape: Two-Dimensional Questions and Possibilities. In *Annual Review of Microbiology, Vol 64, 2010*, Gottesman, S.; Harwood, C. S., Eds. 2010; Vol. 64, pp 223-240.

50. Gon, S.; Fang, B.; Santore, M. M. Interaction of Cationic Proteins and Polypeptides with Biocompatible Cationically-Anchored Peg Brushes Macromolecules 2011, 44, 8161-8168.

51. Gon, S.; Kumar, K. N.; Nusslein, K.; Santore, M. M. How Bacteria Adhere to Brushy Peg Surfaces: Clinging to Flaws and Compressing the Brush Macromolecules 2012, 45, 8373-8381.

52. Kalasin, S.; Browne, E. P.; Arcaro, K. F.; Santore, M. M. Surfaces That Adhesively Discriminate Breast Epithelial Cell Lines and Lymphocytes in Buffer and Human Breast Milk Acs Applied Materials & Interfaces 2019, 11, 16347-16356.

53. Niu, W. A.; Smith, M. N.; Santore, M. M. Depletion Attractions Drive Bacterial Capture on Both Non-Fouling and Adhesive Surfaces, Enhancing Cell Orientation Soft Matter 2022, 10.1039/D2SM01248K.

54. Vigeant, M. A. S.; Wagner, M.; Tamm, L. K.; Ford, R. M. Nanometer Distances between Swimming Bacteria and Surfaces Measured by Total Internal Reflection Aqueous Fluorescence Microscopy Langmuir 2001, 17, 2235-2242.

55. Kurita, T.; Boulanger, P. Computation of Surface Curvature from Range Images Using Geometrically Intrinsic Weights lAPR Workshop on Machine Vision Applications 1992.

56. Harris, C. R.; Millman, K. J.; van der Walt, S. J.; Gommers, R.; Virtanen, P.; Cournapeau, D.; Wieser, E.; Taylor, J.; Berg, S.; Smith, N. J.; Kern, R.; Picus, M.; Hoyer, S.; van Kerkwijk, M. H.; Brett, M.; Haldane, A.; del Rio, J. F.; Wiebe, M.; Peterson, P.; Gerard-Marchant, P.; Sheppard, K.; Reddy, T.; Weckesser, W.; Abbasi, H.; Gohlke, C.; Oliphant, T. E. Array Programming with Numpy Nature 2020, 585, 357-362.

57. Buttrum, S. M.; Hatton, R.; Nash, G. B. Selectin-Mediated Rolling of Neutrophils on Immoblized Platelets Blood 1993, 82, 1165-1174.

58. Lawrence, M. B.; Springer, T. A. Neutrophils Rolls on E-Selectin Journal of Immunology 1993, 151, 6338-6346.

59. Hwang, H.; Paracini, N.; Parks, J. M.; Lakey, J. H.; Gumbart, J. C. Distribution of Mechanical Stress in the Escherichia Coli Cell Envelope Biochimica Et Biophysica Acta-Biomembranes 2018, 1860, 2566-2575.

60. Vaiwala, R.; Sharma, P.; Puranik, M.; Ayappa, K. G. Developing a Coarse-Grained Model for Bacterial Cell Walls: Evaluating Mechanical Properties and Free Energy Barriers Journal of Chemical Theory and Computation 2020, 16, 5369-5384.

61. Rojas, E. R.; Billings, G.; Odermatt, P. D.; Auer, G. K.; Zhu, L.; Miguel, A.; Chang, F.; Weibel, D. B.; Theriot, J. A.; Huang, K. C. The Outer Membrane Is an Essential Load-Bearing Element in Gram-Negative Bacteria Nature 2018, 559, 617-+.